Available online at www.sciencedirect.com
ScienceDirect
Nuclear Instruments and Methods in Physics Research A 586 (2008) 119–123
NUCLEAR INSTRUMENTS & METHODS IN PHYSICS RESEARCH Section A
www.elsevier.com/locate/nima

Perfect crystal neutron interferometry and tensorial neutron tomography

E. Jericha[a,*], R. Szeywerth[b], H. Leeb[a], G. Badurek[a]

[a]*Atominstitut, Vienna University of Technology, Stadionallee 2, 1020 Wien, Austria*
[b]*Institute of Fluid Mechanics and Heat Transfer, Vienna University of Technology, Resselgasse 3, 1040 Wien, Austria*

Available online 26 December 2007

Abstract

Perfect crystal neutron interferometry may be applied in the tomographic study of magnetic structures in ferromagnetic solids. As a result of such investigations one can expect a complete 3D representation of the magnetisation distribution inside the sample. While the concept is comparable to absorption and phase contrast tomography, the tensorial technique involves 3D polarisation control and specific reconstruction algorithms due to path-ordering effects contained in the measured projections. We present the current status of related methodical development and outline the experimental and technical requirements essential for the application of this method. A 2D reconstruction example is given for a standardised simulated test sample using a reconstruction algorithm based on elimination of path-ordering effects by measurements at different neutron velocities.

PACS: 75.60.Ch; 81.70.Tx; 03.75.Dg

Keywords: Neutron depolarisation; Interferometry; Tomography; Magnetic order

1. Introduction

Determination of the magnetic structure of ferromagnetic materials is a particular strength of neutron scattering. In principle, it is possible also to directly visualise the distribution of magnetisation in these materials employing tomographic reconstruction techniques. The experimental realisation of such investigations may be based on polarised neutron optics combined with 3D neutron polarimetry or neutron interferometry. In recent years we have developed several algorithms employing spin rotation in perfect-crystal neutron interferometers to numerically solve the tomographic inversion problem for magnetic samples [1–3]. These concepts are closely related instrumentally and analytically to magnetic phase topography [4] or phase-contrast tomography [5] in perfect-crystal neutron interferometry.

A sketch of the proposed experimental set-up is shown in Fig. 1. The sample is placed in one arm of the interferometer and the interference pattern, generated by an auxiliary phase shifter, spatially resolved with a 2D position sensitive detector. This measurement is performed for a series of different sample rotation angles θ where the rotation axis is assumed to be in the vertical direction running through the centre of the sample. When we consider a specific path $\mathscr{C}_k$ through the sample, the neutrons enter the sample at a horizontal position x_k and at vertical position z_k with the sample rotation set at angle θ_k. Therefore, $\mathscr{C}_k$ is characterised by the coordinates (x_k, z_k, θ_k) and we assume the angular divergence of the neutron beam negligible. Consequently, we will consider a single horizontal plane only, with the z-coordinate fixed at $z = 0$. The description presented here will accordingly apply to each horizontal plane located at different heights z_k.

2. Basic relations and experimental requirements

A tomographic reconstruction is usually performed on a grid consisting of equal size pixels where the unknown quantity, in our case the magnetic field $\boldsymbol{B}_j$ in pixel j, is

*Corresponding author. Tel.: +43 1 58801 14146; fax: +43 1 58801 14199.
E-mail address: jericha@ati.ac.at (E. Jericha).

0168-9002/$ - see front matter © 2007 Elsevier B.V. All rights reserved.
doi:10.1016/j.nima.2007.11.041

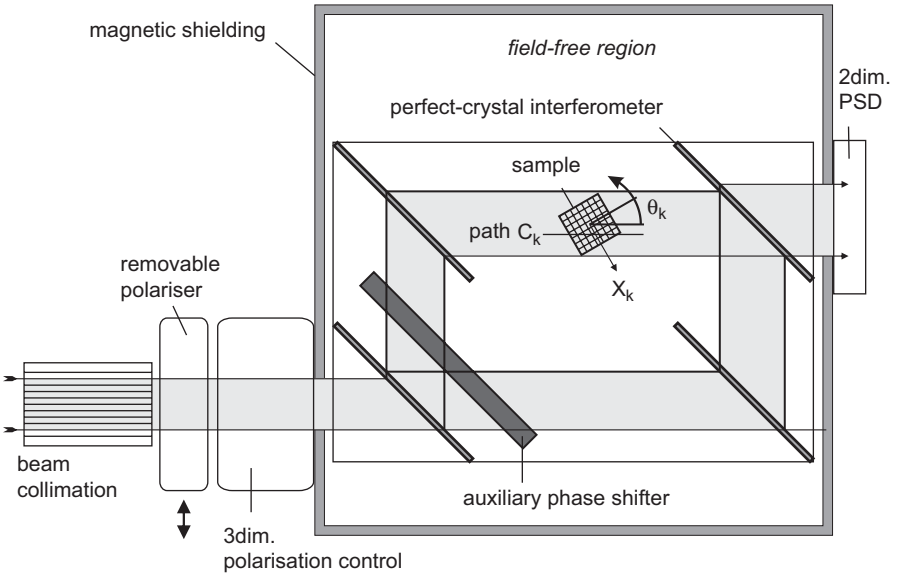

Fig. 1. Sketch of the neutron interferometer set-up proposed for tomographic measurements of magnetic structure. The sample is rotated in one arm of the interferometer and the interference pattern is recorded in a high-resolution 2D position sensitive detector placed in the forward O-direction. Neutron beam preparation consists of beam collimation, and optional polarisation and complete 3D polarisation vector control.

assumed constant. Absorption tomography or phase-contrast tomography depend on simple line-integrals over the pixels along the path $\mathscr{C}_k$, yielding the total attenuation or the total phase shift accumulated on that path, independent of the particular sequence of pixels. On the other hand, in our case we observe the total spin rotation along the path $\mathscr{C}_k$ which depends on the exact sequence of magnetic field strengths and directions along the path. The spin rotation is described by unitary operators $\mathscr{U}'_j$, acting on the neutron wave function on each pixel j. In general, these operators will not commute for arbitrary two pixels. The total spin rotation for path $\mathscr{C}_k$, $\mathscr{U}'_k = \mathscr{U}'_{N_k} \cdot \ldots \cdot \mathscr{U}'_j \cdot \ldots \cdot \mathscr{U}'_1$, will therefore depend on the specific sequence of the operators $\mathscr{U}'_j$, a situation which is described as path-ordering. Tomographic reconstructions, which are denoted as tensorial neutron tomographic techniques in this case, deal with the inversion of projections $\boldsymbol{p}_k$ defined as

$$\boldsymbol{p}_k = \boldsymbol{p}(x_k, \theta_k) = \int_{\mathscr{C}_k}^{\rightarrow} \boldsymbol{B}\,\mathrm{d}s \tag{1}$$

where the arrow on the path integral indicates path-ordering.

The total effect of a ferromagnetic sample on the neutron wave function is described by unitary operators $\mathscr{U}_k$ which contain a scalar phase shift χ_k due to nuclear interaction, and spin rotation due to the interaction with the magnetic field $\boldsymbol{B}$ along the path $\mathscr{C}_k$:

$$\mathscr{U}_k = \exp[\mathrm{i}(\chi_k - \kappa\boldsymbol{\sigma}\cdot\boldsymbol{p}_k] = \mathrm{e}^{\mathrm{i}\chi_k}(s_k\mathbf{1} - \mathrm{i}\boldsymbol{u}_k\cdot\boldsymbol{\sigma}) \tag{2}$$

where $\boldsymbol{\sigma}$ are the Pauli spin matrices, μ_n the neutron magnetic moment, and the parameter $\kappa = |\mu_n|/\hbar v$ is inversely proportional to the neutron velocity v. We identify the scalar $s_k = \cos(\kappa|\boldsymbol{p}_k|)$ and the vector $\boldsymbol{u}_k = \boldsymbol{p}_k \sin(\kappa|\boldsymbol{p}_k|)/|\boldsymbol{p}_k|$ which have the normalisation property

$$s_k^2 + \boldsymbol{u}_k^2 = 1 \tag{3}$$

as a consequence of the unitarity of $\mathscr{U}$.

The neutron intensity at the exit of an ideal interferometer in the forward O-direction results from superposition of the two sub-beams having been spatially separated inside the interferometer and is given by, e.g. Ref. [6],

$$I_O(x_k, \theta_k) = \frac{I_0(x_k)}{2}(1 + s_k\cos\chi_k + (\boldsymbol{P}\cdot\boldsymbol{u}_k)\sin\chi_k) \tag{4}$$

with I_0 the neutron intensity in the empty interferometer and the polarisation $\boldsymbol{P} = \langle\boldsymbol{\sigma}\rangle$ of the incident neutron beam.

For application of this method we follow the arguments in Ref. [5] for interferometer design. The interferometer should have very thin crystal mirror plates to minimise horizontal image smearing, and high accuracy ($\sim$1 μm) of mirror thicknesses and mirror distances for optimum beam focusing on the analyser mirror. While in standard neutron interferometry experiments the interferometer itself selects the degree of angular divergence from the incident wave vector distribution, typically $\sim$10 mrad, a collimation system in front of the instrument is essential to further reduce the effect of horizontal smearing. The degree of collimation depends on the domain sizes under study. Keeping in mind amorphous magnetic ribbons of the type investigated in Ref. [8] among the first applications of this method, the tolerable divergence will be of the order $\sim$1 mrad. On the other end of the instrument a high resolution 2D position sensitive detector is needed since the size of a detector pixel limits the resolvable magnetic domain size. Beside neutron source strength, this

instrument component may turn out to be the critical point in actually realising the technique.

The projections $\boldsymbol{p}_k$ are derived from the interferometrically determined quantities s_k and $\boldsymbol{u}_k$ by $\boldsymbol{p}_k = \boldsymbol{u}_k \arccos s_k/[\kappa \sin(\arccos s_k)]$. To obtain s_k and the three components of $\boldsymbol{u}_k$ we can either use an unpolarised incident beam and full 3D polarisation analysis of the outgoing beam [1,2], an incident beam with fixed polarisation and polarisation analysis of the outgoing beam [7] or full polarisation control over the incident beam and no polarisation analysis of the outgoing beam as shown in Fig. 1. This last configuration is particularly preferable since it keeps the distance between sample and detector short. Even in case of small angular divergence the intensity cannot be arbitrarily reduced in order to record a spatially resolved interference pattern in reasonable measuring time under stable interferometer conditions. A minimum distance between sample and detector consequently allows to minimise horizontal smearing effects from residual beam divergence.

When we choose three orthogonal polarisation directions which coincide with the axes of our coordinate system, $i = x, y, z$, we obtain in the O-detector the intensities I_{unpol} for the unpolarised incident beam and $I^{(i)}_{\text{pol}}$ for an incident beam polarised in i-direction:

$$I_{\text{unpol}}(x_k, \theta_k) = \frac{I_0(x_k)}{2}(1 + s_k \cos\chi_k)$$
$$I^{(i)}_{\text{pol}}(x_k, \theta_k) = \frac{I'_0(x_k)}{2}(1 + s_k \cos\chi_k + P_i u_{ki} \sin\chi_k) \quad (5)$$

where the unpolarised neutron intensity in the empty interferometer is denoted as I_0 and the polarised intensity, which will in general be different from I_0, as I'_0. We derive the quantities s_k and $\boldsymbol{u}_k$ from these intensities:

$$s_k = \frac{1}{\cos\chi_k}\left(\frac{2I_{\text{unpol}}(x_k, \theta_k)}{I_0(x_k)} - 1\right)$$
$$u_{ki} = \frac{2}{P_i \sin\chi_k}\left(\frac{I^{(i)}_{\text{pol}}(x_k, \theta_k)}{I'_0(x_k)} - \frac{I_{\text{unpol}}(x_k, \theta_k)}{I_0(x_k)}\right). \quad (6)$$

An additional equation is required for the phase shift χ_k which may be calculated from sample parameters and data tables, and with relation (3) which constrains the values of s_k, $\boldsymbol{u}_k$ and χ_k. For an essentially homogeneous sample $\chi_k = -\lambda N b_c d_k$ with the neutron wavelength λ, the coherent nuclear scattering length density Nb_c, and d_k the length of path $\mathscr{C}_k$. It will depend on the specific experimental situation whether values from data tables will provide higher accuracy compared with experimental errors, or unknown sample inhomogeneities or path length uncertainties will render calculations impossible and require an experimental determination.

In Ref. [6] it was found that a guide field and ambient magnetic fields cause additional spin rotation which in general is not known well enough to extract the relevant quantities from the interference patterns. This additional spin rotation can be eliminated by placing the neutron beam path inside a magnetic shielding after preparation of the neutron beam polarisation, i.e. by placing the interferometer in a magnetic field-free region. For experimental realisation we imagine a zero field polarimeter of the MuPAD or CRYOPAD type [9].

3. Data reconstruction by elimination of path-ordering effects

In recent years we have developed a series of different reconstruction algorithms mainly based on iteration procedures. We considered separation of line integrals and path-ordering effects, where the line integrals are inverted by standard inverse Radon transformation methods, e.g. Ref. [10], and path-ordering is taken into account by a correction term whose convergence is sought via an iteration procedure [1]. This method was improved to a sum of separated logarithms algorithm which takes care of non-vanishing commutator terms [2]. Contrary to the idea of separating the effects of path-ordering, it is possible to incorporate them directly into the reconstruction algorithm which is realised by modified algebraic reconstruction techniques (ARTs) [3]. Yet another possibility for data reconstruction is the elimination of path-ordering effects when measuring at different neutron velocities.

To sketch this method we write the projections $\boldsymbol{p}_k$ as power series in κ, or equivalently $1/v$,

$$\boldsymbol{p}_k(v) = \sum_{l=0}^{\infty} \kappa^l \boldsymbol{b}^{(l)}(x_k, \theta_k). \quad (7)$$

We find that the coefficient $\boldsymbol{b}^{(0)}_k = \boldsymbol{b}^{(0)}(x_k, \theta_k)$ corresponds exactly to the line integral $\int_{\mathscr{C}_k} \boldsymbol{B}\,\mathrm{d}s$ without any contributions from path-ordering. These line integrals may be inverted e.g. by filtered backprojection (FBP) or an iterative ART. The aim of the elimination procedure is to eliminate as many terms with exponent $l>0$ from the series as possible. An important step considers the equations for $-\kappa$ instead of κ. We observe that in this case $\mathscr{U}_j$ is replaced by its adjoint operator $\mathscr{U}^\dagger_j$ and $\mathscr{U}$ by

$$\mathscr{U}(-\kappa) = \prod_{j=1}^{N_k} \mathscr{U}^\dagger_j = \left(\prod_{j=N_k}^{1} \mathscr{U}_j\right)^\dagger = \bar{\mathscr{U}}^\dagger(\kappa) \quad (8)$$

where N_k is the number of pixels along the path $\mathscr{C}_k$. The adjoint path traverses the sample in exactly the reverse order of pixels than the original path. From the point of sample rotation it coincides with angle $\theta_k + \pi$ compared to the original angle θ_k. Inserting the power series (7) into Eq. (8) we obtain

$$\mathscr{U}(-\kappa) = \exp\left[\mathrm{i}\kappa\boldsymbol{\sigma} \cdot \sum_l (-\kappa)^l \boldsymbol{b}^{(l)}(x_k, \theta_k)\right]$$
$$= \bar{\mathscr{U}}^\dagger(\kappa) = \exp\left[\mathrm{i}\kappa\boldsymbol{\sigma} \cdot \sum_l \kappa^l \boldsymbol{b}^{(l)}(x_k, \theta_k + \pi)\right]$$

and we find for the adjoint path the expansion

$$\boldsymbol{p}(x_k,\theta_k+\pi)=\sum_{l=0}^{\infty}(-\kappa)^l\boldsymbol{b}^{(l)}(x_k,\theta_k). \tag{9}$$

Adding the two series (7) and (9) and dividing the sum by 2 we further obtain

$$\bar{\boldsymbol{p}}_k(v)=\sum_{l=0}^{\infty}\kappa^{2l}\boldsymbol{b}_k^{(2l)} \tag{10}$$

where all odd orders in κ have been eliminated. If we neglect all orders larger than κ^2 we find the line integral $\boldsymbol{b}_k^{(0)}$ by measuring at two different neutron velocities v_1 and v_2 as

$$\int_{\mathscr{C}_k}\boldsymbol{B}\,\mathrm{d}s=\boldsymbol{b}_k^{(0)}=\frac{v_1^2\bar{\boldsymbol{p}}_k(v_1)-v_2^2\bar{\boldsymbol{p}}_k(v_2)}{v_1^2-v_2^2}. \tag{11}$$

This concept can be extended to n measurements at n different velocities. If we neglect terms of the order κ^{2n} and higher we find a polynomial of order $n-1$ for the projections $\bar{\boldsymbol{p}}_k(v)$ with $l=n-1$ as upper limit for the sum in Eq. (10). To obtain again the line-integral we make use of Lagrange's interpolation polynomial of order $n-1$

$$\bar{\boldsymbol{p}}_k(v)=\sum_{h=1}^{n}\prod_{m\neq h}\frac{\kappa-\kappa_m}{\kappa_h-\kappa_m}\bar{\boldsymbol{p}}_k(v_h). \tag{12}$$

For $\kappa\to 0$, $\bar{\boldsymbol{p}}_k$ approaches $\boldsymbol{b}_k^{(0)}$ and we find from Eq. (12)

$$\boldsymbol{b}_k^{(0)}=\sum_{h=1}^{n}\prod_{m\neq h}\frac{\kappa_m}{\kappa_m-\kappa_h}\bar{\boldsymbol{p}}_k(v_h) \tag{13}$$

and the weighting factors for the projections $\bar{\boldsymbol{p}}_k(v_h)$ measured at velocity v_h are

$$g_h=\prod_{m\neq h}\frac{v_h^2}{v_h^2-v_m^2} \tag{14}$$

in agreement with Eq. (11) and thus

$$\int_{\mathscr{C}_k}\boldsymbol{B}\,\mathrm{d}s=\sum_{h=1}^{n}g_h\left(\int_{\mathscr{C}_k}^{\rightarrow}\boldsymbol{B}\,\mathrm{d}s\right)(v_h). \tag{15}$$

Now, we apply a standard inverse Radon transformation $\mathscr{R}^{-1}$ to derive the sample magnetisation

$$\boldsymbol{B}=\mathscr{R}^{-1}\left(\int\boldsymbol{B}\,\mathrm{d}s\right)=\sum_{h=1}^{n}g_h\mathscr{R}^{-1}\left(\int^{\rightarrow}\boldsymbol{B}\,\mathrm{d}s\right)(v_h). \tag{16}$$

Due to the properties of the inverse Radon transformation, see e.g. Ref. [10], it is formally equivalent to perform it on the weighted sum on the right side of Eq. (15) or on the measured projections $\bar{\boldsymbol{p}}(v_h)$ prior to calculating the weighted sum.

4. Model sample reconstruction

Fig. 2 shows a model sample which was introduced in Ref. [1] to assess the quality of our reconstruction algorithms and subsequently used for the algorithms presented in Refs. [2,3]. The structure consists of 20×20 pixels whose linear dimensions are varied to check the performance of the algorithms with growing pixel size. This is important for experimental realisation—specifically when one considers the minimum pixel size feasible for a 2D PSD.

For this sample we calculate a number of projections along different paths $\mathscr{C}_k$ at various sample rotation angles θ_k. These projections correspond to the recorded data in a real experiment. Similar to the uncertainties in an experiment we may also add statistical fluctuations to our calculated data.

The quality of the reconstruction is shown in Fig. 3 for $n=2,3,4$ different velocities and was calculated by ART with $v=10$ iteration steps per grid size. The quality is defined as the *rms* deviation of the reconstruction from the original magnetisation distribution

$$\Delta=\sqrt{\frac{1}{N}\sum_{j=1}^{N}|\boldsymbol{B}_j-\boldsymbol{B}_j^{(v)}|^2} \tag{17}$$

averaged over all N pixels in the sample. This method yields good results up to a pixel size of about 6–7 μm which is superior to most of the algorithms presented in Refs. [1–3]. Furthermore, a particular strength of this

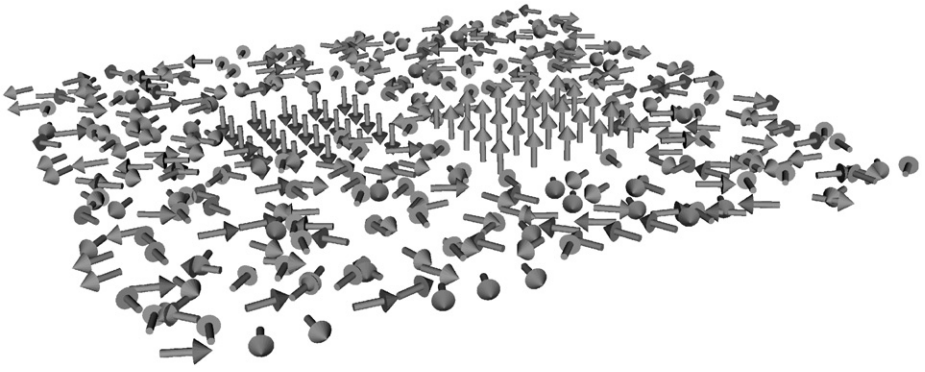

Fig. 2. This virtual sample has become our standard test sample and was already used in Refs. [1–3] to compare different reconstruction algorithms. It consists of a 20×20 pixel structure. The magnetisation in each pixel is 1 T.

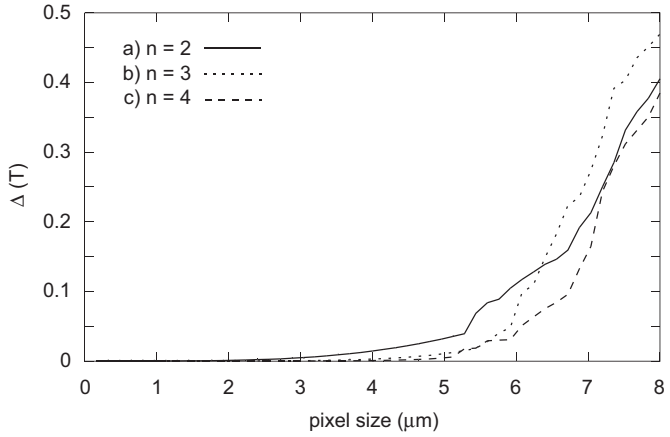

Fig. 3. Reconstruction quality for $n = 2, 3, 4$ different velocities, $v_1 = 2000\,\mathrm{m/s}$, $v_n = 3000\,\mathrm{m/s}$. Path-ordering effects were eliminated by procedure (15) and the magnetisation distribution calculated from the resulting projections by Eq. (16) employing an iterative algebraic reconstruction technique (ART) with 10 iterations per grid size.

method is its independence of any model assumptions which are needed for reconstruction by other techniques.

At larger pixel size the influence of higher order path-ordering effects and ambiguities due to spin rotation angles larger than 2π cause deteriorations of the reconstruction. Fig. 3 is based on calculations where we assumed good counting statistics and modest experimental error. It turns out that the elimination technique is rather sensitive to increasing statistical fluctuations. We see from Eq. (15) that the experimental errors of all the projections experimentally determined at different velocities are weighted and added during the elimination procedure. In the case that the different velocities are close to each other the weighting factors g_h become rather large with a corresponding effect on experimental errors. From a technical point of view the sensitivity to large statistical uncertainties are explained by the then ill-defined interpolation procedure (13).

5. Conclusions

We have developed an algorithm for tensorial neutron tomographic reconstruction of magnetisation distributions in ferromagnetic samples based on measurements at different neutron velocities. This method gives reasonable results up to relatively large pixel sizes of the grid on which the reconstruction is performed. The concept and implementation of the algorithm are straightforward and compare well to results from methods presented in Refs. [1–3]. Together these algorithms represent a powerful set of possible reconstruction techniques for tensorial tomographic problems.

We expect that further development of such techniques will be based on combined methods employing modified ART and measurements at different neutron velocities. This latter point suggests to consider a related experiment located at a pulsed neutron spallation source. Due to the characteristics of the interferometric measurements this application would ask for a high intensity long-pulse option for the spallation source and experiments would make use of different Bragg reflection orders like $(2, 2, 0)$, $(4, 4, 0)$ and so forth, simultaneously.

Acknowledgements

This research project has been supported by the European Commission under the 6th Framework Programme through the Key Action: Strengthening the European Research Area, Research Infrastructures. Contract no: RII3-CT-2003-505925.

References

[1] G. Badurek, R.J. Buchelt, H. Leeb, R. Szeywerth, Physica B 335 (2003) 114.
[2] H. Leeb, R. Szeywerth, E. Jericha, G. Badurek, Physica B 356 (2005) 187.
[3] E. Jericha, R. Szeywerth, H. Leeb, G. Badurek, Physica B 397 (2007) 159.
[4] M. Schlenker, W. Bauspiess, W. Graeff, U. Bonse, H. Rauch, J. Magn. Mater. 15–18 (1980) 1507.
[5] F. Dubus, U. Bonse, M. Zawisky, M. Baron, R. Loidl, IEEE Trans. Nucl. Sci. NS-52 (2005) 364.
[6] G. Badurek, R.J. Buchelt, H. Leeb, Physica B 350 (2004) e1047.
[7] G. Badurek, R.J. Buchelt, H. Leeb, Physica B 276–278 (2000) 588.
[8] A. Veider, G. Badurek, R. Grössinger, H. Kronmüller, J. Magn. Magn. Mater. 60 (1986) 182.
[9] E. Lelièvre-Berna, P.J. Brown, F. Tasset, K. Kakurai, M. Takeda, L.-P. Regnault, Physica B 397 (2007) 120.
[10] H.H. Barrett, W. Swindell, Radiologic Imaging, Academic Press, New York, 1981.